Monitoring battery electrolyte chemistry via in-operando tilted fiber Bragg grating sensors

Jiaqiang Huang, Xile Han, Fu Liu, Charlotte Gervillié, Laura Albero Blanquer, Tuan Guo, Jean-Marie Tarascon

ARTICLE

Monitoring battery electrolyte chemistry via in-operando tilted fiber Bragg grating sensors

Received 00th January 20xx,
Accepted 00th January 20xx

DOI: 10.1039/x0xx00000x

Jiaqiang Huang,[ab] Xile Han,[c] Fu Liu,[d] Charlotte Gervillié,[ab] Laura Albero Blanquer,[abe] Tuan Guo*[c] and Jean-Marie Tarascon*[abe]

Operando tracking the chemical dynamics/states of a battery and its components is critical to their second life for boosting their sustainability. Herein, we demonstrate the feasibility and diversity of the tilted fiber Bragg grating (TFBG) optical fiber sensors to operando access the chemistry and states of electrolytes. We show how a single TFBG sensor can simultaneously measure the temperature and refractive index evolution inside the batteries, which pertains to the chemical evolution of the electrolyte. We also, for the first time, monitor the turbidity of electrolytes via the particulate-induced optical scattering and absorption. These unravelled electrolyte characteristics by TFBG help determine the electrochemical reaction pathways, while strongly correlated to the capacity loss. This type of sensing offers intriguing opportunities to building a "lab-on-fiber" platform for deeper chemistry and practical applications, provided we can delicately converge electrochemistry, photonics, and data science.

Introduction

Batteries are essential energy storage devices in the transition from fossil fuel towards sustainable energy[1]. Their rapid market growth driven by the increasing popularity of electric vehicles raises concerns about their sustainability. Besides securing recycling[2], extending the lifetime of batteries and ensuring their second life become increasingly critical for enhancing their greenness. To meet such objectives, accurate monitoring of their state of health becomes a must[3].

Considerable efforts have been placed in the quest for new diagnostic techniques[4] beyond the use of current and voltage or the positioning of a few thermal probes in the latest electric vehicles. Generic lithium- and sodium-ion batteries consist of two electrodes immersed in a liquid electrolyte. Nowadays, numerous techniques can operando track batteries in real working conditions by monitoring heat flow via the isothermal calorimetry[5] or follow the electrode cracking by either acoustic[6] or optic[7] means. In contrast, only a few can operando monitor the electrochemical stability of liquid electrolyte that mainly governs the nucleation and growth of solid electrolyte interphase (SEI),[8, 9] which largely influences the lifetime of batteries[8-10]. Methods such as infrared spectroscopy[11], mass spectrometry[11], and nuclear magnetic resonance[12] provide valuable information about electrolyte decomposition. However, such techniques usually required post-mortem analysis or specific cell designs that take us away from battery operation in the real world. Recently, Dahn *et al.* showed that differential thermal analysis (DTA) is useful to examine the composition of electrolytes[13] but also reported how acoustic transmission mapping can *in situ* probe the electrolyte depletion[14, 15]. Nevertheless, to be implemented in electric vehicles, these two methods still need to overcome a few challenges, such as the cumbersome DTA apparatus or the liquid coupling agent for acoustics[15]. Recently, we have been witnessing the ingress of optical fiber sensors, because of their low-invasiveness, smallness, electromagnetic immunity, and insulator nature, as promising candidates to study electrolyte degradation by exploiting the interaction of the light carried by the fiber with its surrounding chemical environment.

We previously demonstrated the use of fiber Bragg grating (FBG) sensors, inscribed either in single-mode fiber (SMF) or in microstructured fiber (MOF) that was placed inside a battery, to monitor changes in multiple parameters such as temperature (*T*) and pressure (*P*) in real-world conditions[4, 16] with high sensitivity and space resolution[17]. However, in such a configuration, the fiber acts as a true waveguide with the traveling light being fully transparent to the fiber-surrounding environment. Nonetheless, this limitation can be bypassed by modifying the structure of the fibers to obtain either cladding-etched fibers for optic evanescent wave spectroscopy[18] or hollow-core fibers with pumped electrolyte for Raman spectroscopy[19]. Besides, increasing the grating period (~500 nm to ~500 µm) and tilting the grating plane of FBGs leads to two other types of sensors called LPG for long-period grating sensing and TFBG for tilted fiber Bragg grating, respectively. Both

[a] Chimie du Solide et de l'Energie, UMR 8260 CNRS, Collège de France, 75005 Paris, France. Email: jean-marie.tarascon@college-de-france.fr
[b] Réseau sur le Stockage Electrochimique de l'Energie (RS2E), FR CNRS 3459, 80039 Amiens, France.
[c] Institute of Photonics Technology, Jinan University, Guangzhou 510632, China. Email: tuanguo@jnu.edu.cn
[d] Department of Electronics, Carleton University, Ottawa, K1S 5B6, Canada.
[e] Sorbonne Université, UPMC Paris 06, 75005 Paris, France.

†Electronic Supplementary Information (ESI) available: [details of any supplementary information available should be included here]. See DOI: 10.1039/x0xx00000x

provide the advantage of coupling the core mode and the cladding modes[20, 21]. Bearing in mind that the light of cladding modes is penetrating the fiber environment, LPG and TFBG are sensitive to the surrounding refractive index (*RI*), hence enabling their real applications in (bio-)chemical sensing[21-23] and their onset within the field of electrochemistry[24] such as supercapacitors[25].

Progress in this direction is illustrated by a recent study dealing with *RI* measurements conducted in pouch cells via the use of an FBG sensor inscribed into the etched cladding of an optical fiber[26]. However, with this approach, several intertwined parameters (*T*, *RI*, and ε) are measured at once, hence rendering the quantification infeasible[26]. To contour this complexity and explicitly link the *RI* with the underlying chemistries, we decided to implement the injection of TFBGs into cylindrical cells[4] to remove the sensibility to ε. Unlike the solely peak pertaining to FBG and LPG detection, the rich features in TFBG's spectra facilitate the decoupling of multiple parameters such as *T* and *RI*. In addition, inscribed in commercial SMFs, TFBG gets rid of the intricate processes of hydrofluoric acid etching[18, 26] or microstructural fiber fabrication[19].

Herein, we explore the application of TFBG for monitoring in operando mode the electrolyte degradations of batteries. We first introduce the working principle of TFBG and its spectral characteristics in response to perturbations (*RI*, *T*, ε, and *P*). For proof of concept, we select studying the $Na_3V_2(PO_4)_2F_3$/hard carbon (NVPF/HC) Na-ion electrochemistry in 18650 cells containing various electrolyte combinations. We demonstrate the capability of a single TFBG to operando monitor *T* and *RI* simultaneously inside the battery. By exploiting the time-resolved *RI* signals, we illustrate the feasibility of tracking electrolyte deterioration while accessing the turbidity of electrolytes as well. Lastly, we prove that TFBG-based observables are not only helpful in verifying the proposed mechanisms of SEI formation but also correlated to the cell capacity loss, thus offering additional metrics to monitor the state of health of batteries.

Results

From an experimental standpoint, the use of optical sensing and namely TFBGs is novel within the battery community; hence we decided at first to briefly recall the fundamental science beyond it together with means to calibrate, collect, read, and exploit optical signals to access various observables, prior to moving to the implementation of TFBG's sensors for in operando battery inspection.

Sensing theory of TFBG

Fig. 1a and b show the schematics of a FBG and a TFBG, respectively. Differing from FBG, the TFBGs' grating plane is rotated around an axis perpendicular to the fiber axis by an angle, which ensures the coupling between the single forward-propagating core mode and a larger number of backward propagating cladding modes (dips in Fig. 1b and 2a) through the phase matching relation[21, 27]:

$$\lambda_{clad}(i) = \left(n_{eff}(i) + n_{eff,clad}(i)\right)\Lambda/\cos\theta \qquad (1)$$

where $\lambda_{clad}(i)$ is the corresponding wavelength of the i^{th} order cladding mode, $n_{eff}(i)$ is the effective refractive index of the core mode at $\lambda_{clad}(i)$, $n_{eff,clad}(i)$ is the i^{th} order cladding mode's effective refractive index, Λ is the period of the interference pattern creating the grating, and θ is the tilting angle of grating planes relative to the cross section of the fiber. Upon any perturbation in the external medium's refractive index (or permittivity), these discrete cladding mode resonances shift in wavelength and/or amplitude, because the evanescent field of the cladding modes (purple arrows in Fig. 1b) can penetrate and interact with the surrounding (*i.e.*, "Electrolyte" in Fig. 1b), enabling spatial monitoring. Meanwhile, the Bragg resonance exists for both FBG and TFBG as shown by the peak in Fig. 1a and 2a, whose wavelength (λ_B) is defined by

$$\lambda_B = 2n_{eff}\Lambda/cos\theta \qquad (2)$$

where n_{eff} is the effective refractive index of the core at λ_B. Since the effective refractive indices ($n_{eff}(i)$, $n_{eff,clad}(i)$, n_{eff}) of core and cladding modes together with the grating period (Λ) are strongly dependent on *T*, ε, and *P*, the λ_B is sensitive to these perturbations.

Sensitivities of TFBG to *RI*, *T*, ε, and *P*

A thin gold layer was coated on one end of TFBG by magnetron sputtering to obtain a sensing probe working in the reflection mode (Fig. 1b) for the read-out of an optical interrogator (si255, LUNA). To decouple the multiple perturbations sensed by TFBG,

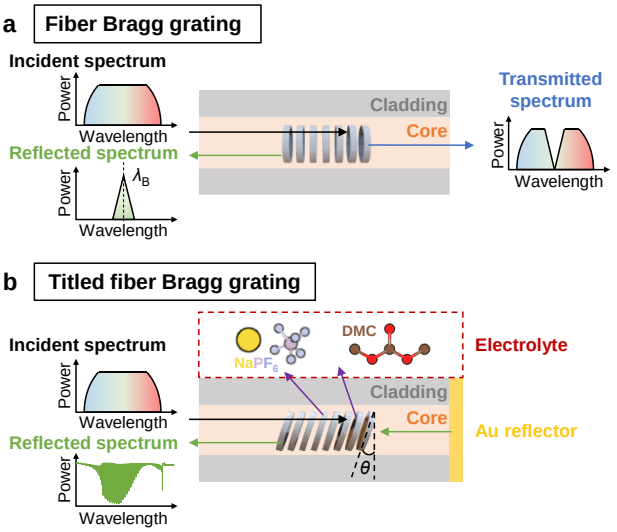

Fig. 1 Concepts of FBG and TFBG. (a and b) Schematics and spectra of a FBG (a) and a TFBG (b). The grating plane of TFBG was tilted at an angle of θ with respect to the perpendicular of the fiber axis. A gold layer ("Au reflector" in b) was deposited on the end of TFBG to obtain the reflection probe (green arrows in b). The incident light with wavelength ranging from 1,500 to 1,600 nm was injected into FBG and TFBG (black arrows in a and b). As for FBG in (a), the light was largely confined inside the fiber core, and the backward coupled core mode gives rise to a peak and a dip in reflected and transmitted spectra, respectively[21]. Turning to TFBG in (b), the light from the propagating core mode couples with the backward cladding modes (purple arrows), exhibiting numerous resonances (dips) in the collected spectrum, see the enlarged one in Fig. 2a. The evanescent field of these cladding modes can penetrate and interact with the surrounding (*i.e.*, "Electrolyte" in b), rendering the sensitivity to surrounding refractive index.

we firstly measured its spectrum response to a single variable parameter.

Starting from *RI*, the TFBG was thoroughly immersed in series of sucrose aqueous solutions ranging from 0 to 50 wt.%, and the reflection spectra were collected at 2 wt.% intervals. The refractive indices of the solutions were benchmarked by a commercial refractometer (AR200, Reichert Technologies; resolution: ±0.0001 refractive index unit (RIU)), revealing *RI* increases with the concentration of sucrose (Fig. S1). Fig. 2a shows spectra for a TFBG sensor in 10 wt.% sucrose solution (top) and greater sucrose contents (bottom). They all display a low-amplitude Bragg peak at the longest wavelength (Fig. 2a, red-shaded region) and tens of high-amplitude dips at shorter wavelengths. These dips are further classified into the leaky mode (Fig. 2a, grey-shaded region) and guided cladding mode (Fig. 2a, yellow-shaded region) resonances[21], between which is the so-called "cut-off" mode[21] (~1,526 nm in Fig. 2a). The leaky modes are distinguished from the guided cladding modes by the sharp decreases in the resonance amplitudes, because their $n_{eff,clad}(i)$ is lower than the surrounding refractive index so that the total internal reflection is lost[21]. As expected, by increasing the sucrose concentration (*i.e.*, *RI*) in Fig. 2a (bottom), more and more resonances at shorter wavelengths are suppressed in amplitude, namely, become leaky. To

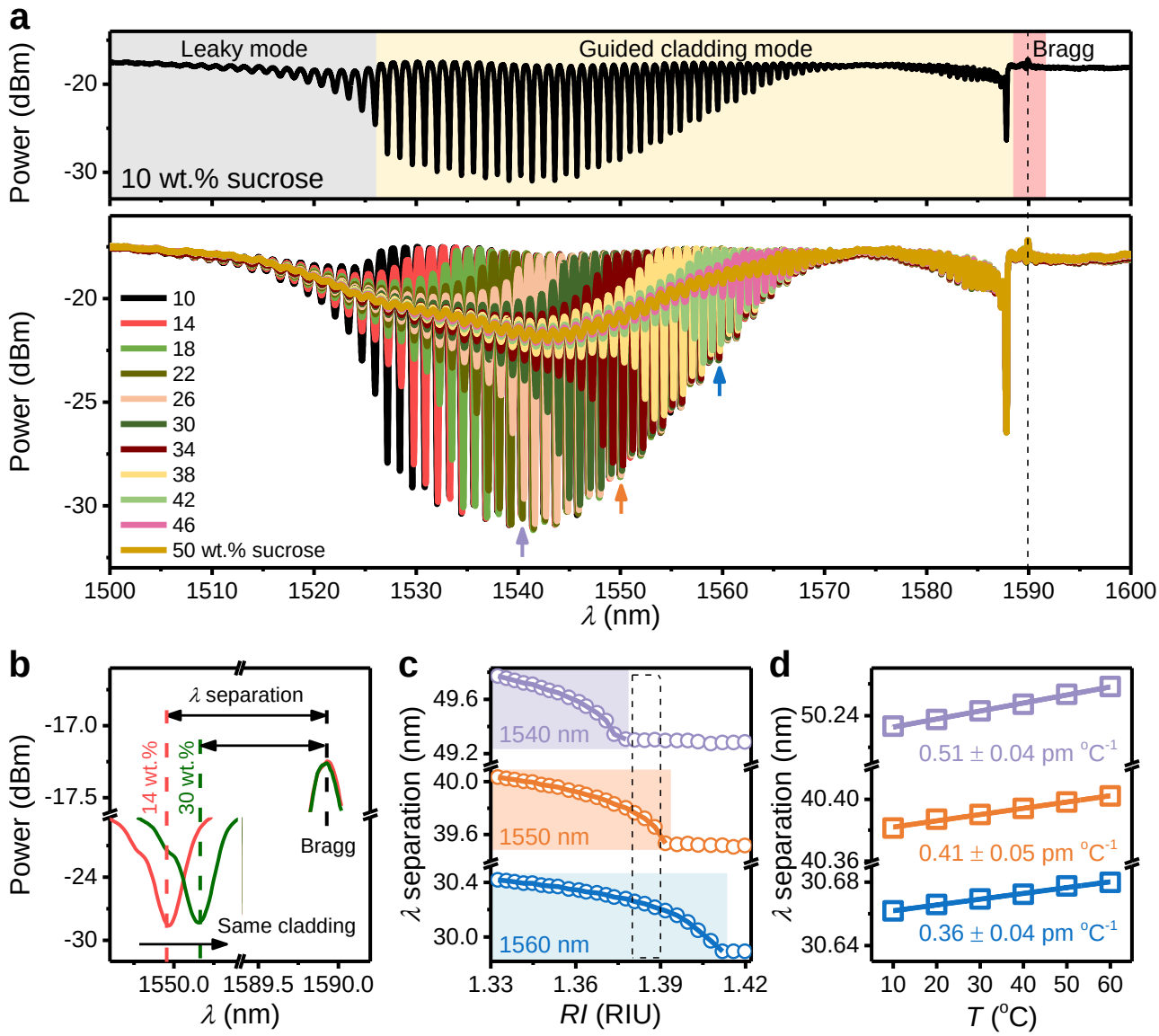

Fig. 2 Calibrations of TFBG. (a) The spectra of TFBG immersed in sucrose solutions with concentrations ranging from 10 to 50 wt.%. The top panel shows the individual spectra in 10 wt.% sucrose solution, where the leaky mode, guided cladding mode, and Bragg resonances are shaded by grey, yellow, and red, respectively. To visualize more features in the limited space, only 11 spectra are present. The grey, orange, and blue arrows indicate the three resonances in (c and d), while the black dash line corresponds to the Bragg resonance. The high-amplitude dip at 1,588 nm is called the "ghost" mode[21]. (b) The wavelength shift of a cladding resonance at ~1,550 nm in response to the sucrose concentration variation from 14 to 30 wt.%. The wavelength (λ) separations between the cladding and Bragg resonances are marked. (c and d) The wavelength separations between the Bragg and three cladding resonances at ~1,560 (blue), ~1,550 (orange), and ~1,540 (purple) nm as a function of *RI* (c) and *T* (d). Note that the *RI* increases with sucrose concentration. While scatters represent the raw data, the solid lines in (c and d) indicate the linear interpolation and linear regression (with the slopes), respectively. The uncertainty of the slope in (d) is given by three standard deviations (±3σ). The region, where the wavelength separation varies with *RI*, is shaded as the response ranges in (c). The dashed rectangle in (c) indicates the example measurement range between 1.38 to 1.39 RIU as discussed.

examine the wavelength shifts, we selected two sucrose concentrations (14 and 30 wt.%) and zoomed in one dip at ~1,550 nm together with the Bragg resonance in Fig. 2b. The dip shifts its wavelength by 213 pm, because the evanescent field penetration of the cladding mode (into the surrounding media) goes up from 14 to 30 wt.% sucrose concentration, leading to the increase of $n_{eff,clad}(i)$ and $\lambda_{clad}(i)$ in eqn (1). On the contrary, the Bragg resonance remains invariant with *RI* in Fig. 2b and thus can be used as a stable power and wavelength reference[19]. Therefore, we use the wavelength separation (Fig. 2b and c) between the cladding and Bragg resonances[27] to monitor *RI* rather than the solely cladding wavelength. Fig. 2c further shows wavelength separations of three different resonances in response to *RI*. Interestingly, the wavelength separations vary with *RI* (in response range, shaded regions in Fig. 2c) and remain constant after a specified *RI* (unshaded data in Fig. 2c). The constancy of wavelength separations is associated with the transition from the guided to leaky mode, as discussed in Fig. 2a.

An immediate question is how to select the appropriate resonance for *RI* measurement. Two criteria matter: the working range and the sensitivity. For example, in one measurement, the *RI* of electrolyte varies between 1.38 and 1.39 RIU, that is, the working range (dashed rectangle in Fig. 2c). To have a response within the working range, we can directly exclude the 1,540-nm resonance in Fig. 2c because of its response range below 1.38 RIU. Next to select the proper resonance from the remaining ones in Fig. 2c, we examined their sensitivities in the working range via dividing the shift in wavelength separation by the *RI* change, namely, -18.0 (-0.180/0.01) and -6.5 (-0.065/0.01) nm RIU^{-1} for 1,550- and 1,560-nm resonances, respectively. For better sensitivity, the 1,550-nm resonance was eventually chosen. In this case, given the 1-pm accuracy of the interrogator, we expected a *RI* resolution of |(1 pm) / (-18 nm RIU^{-1})|, namely, 6×10^{-5} RIU.

To interrogate the TFBG's response to *T*, a TFBG was placed into an oven, and the temperature was changed from 10 to 60 °C with a step of 10 °C and a rest time of 4 hours in each step. The collected spectra, once thermal equilibrium was achieved, are shown in Fig. S2. They show a redshift of the resonances with temperature (Fig. S2b). Moreover, the thermal sensitivity (k_T) linearly increases with the wavelength in the range of 9.2 and 10.1 pm $°C^{-1}$ (Fig. S2d). Though usually ignored[27], the wavelength separation grows slightly and linearly with the temperature (Fig. 2d, <1 pm $°C^{-1}$), which we will consider in this work.

We also examined the responses of TFBG to ε and *P* (Fig. S3 and S4), see details in Methods. The wavelengths redshift and blueshift in response to ε and *P*, respectively. Among these two perturbations, the rate constant response of ε (k_ε) increases with wavelength (Fig. S3d), leading to the increase of wavelength separation with ε (Fig. S3e). On the contrary, we could not spot a clear trend of the rate constant response to *P* (k_P) as a function of wavelength (Fig. S4d) within the 20-bar range (the limit of the safety device of 18650 cells); hence the effect of *P* will be excluded from our data analysis.

_T_ and _RI_ dynamics in 18650 cells unravelled by TFBG

We inserted the TFBG sensor into the central void of the jelly roll of NVPF/HC 18650 cells[4] (Fig. 3a), thus removing the sensibility to ε. Consequently, having excluded the effect of both ε and *P*, changes in the collected spectra will be from now on ascribed to variations of *T* and *RI*. For proof of concept, we started with the simplest electrolyte formula, 1 M $NaPF_6$ in dimethyl carbonate (denoted as "$NaPF_6$/DMC"), which was injected through the same hole that for the sensor (Fig. 3a). Fig. 3b shows the voltage profile (top) and the TFBG spectrum evolution (middle and bottom) during the first charge at C/10. Distinguishable amplitude and wavelength changes are seen in the enlarged contour (Fig. 3b, bottom). For example, towards the end of charge, the resonance amplitude at 1538.8 nm decreases together with the wavelength redshift at 1541 nm. To further visualize the spectrum evolution, we evenly selected five points (Fig. 3b, scatters) and presented their spectra in Fig. 3c and d. Amplitude changes of leaky modes together with the wavelength shifts of guided cladding modes are clearly seen, implying the *RI* variation of electrolyte upon the charging process.

To decrypt the information hidden in the signals, we firstly calculated *T* (Fig. 3e, top) from the Bragg wavelength shifts ($\Delta\lambda_B$) by $T = T_0 + \Delta\lambda_B/k_T$ (with T_0 being the oven temperature (25 °C) and k_T being the thermal sensitivity in Fig. S2c, black), because the Bragg resonance is immune to *RI* change (Fig. 2b). For decoding *RI*, we then selected a cladding mode according to two criteria (the working range and the sensitivity) as discussed previously. The wavelength separations of the cladding were measured as done in Fig. 2b. To avoid the possible drifts of TFBG (Fig. S5a), we mimicked the procedure of the commercial refractometer (*i.e.*, calibration against distilled water before measurements) and corrected the TFBG against the *RI* of pristine electrolyte. Namely, the wavelength separations were corrected to ensure the measured *RI* by the TFBG before charging is equal to the electrolyte's *RI* given by the commercial refractometer. This correction method is described in detail and tested in Fig. S5. We thus obtained the corrected wavelength separation (Fig. 3e, middle). We further removed the minor variation of wavelength separation due to temperature (Fig. 2d) and calculated the *RI* (Fig. 3e, bottom, black line) according to the established calibration curves as shown in Fig. 2c. However, besides the intrinsic temperature dependence of TFBG, the *RI* itself is also influenced by temperature[28, 29], pressure[28], and composition of the electrolyte[29]. To gain the desired composition information of electrolyte, we thus measured the temperature coefficient of *RI* (d*RI*/d*T*) of the electrolyte (Fig. S6, see details in Methods), namely, -6.85×10^{-4} RIU $°C^{-1}$ for $NaPF_6$/DMC, and removed the *T*-induced *RI* change (Fig. 3e, bottom, purple line) by $RI' = RI - (T - T_0)*dRI/dT$. Regarding the pressure, we cannot experimentally measure the pressure coefficient of *RI* (d*RI*/d*P*) of the electrolyte but found that the d*RI*/d*P* of liquids (benzene, carbon tetrachloride, and water)[28] ranges typically from 1×10^{-5} to 5×10^{-5} RIU bar^{-1}. Considering the pressure of <5 bar inside the cell[4], we neglected the d*RI*/d*P* afterward. Consequently, the changes of *RI*' (Fig. 3e, bottom,

purple line) stems mostly from the electrolyte composition evolution.

We further examined the repeatability of TFBG measurements in the first two formation cycles (Fig. 3f, shadings for error bars). While the time-resolved voltage and *T* profiles deliver negligible error bars (Fig. 3f, top and middle, shadings), the *RI*' results manifest considerate error bars in the first charge (Fig. 3f, bottom, shading). Surprisingly, the significant error bars of *RI*' immediately decrease after the cell resting period, implying that its origin is most likely nested in kinetics- or diffusion-driven issues rather than in an experimental artefact, and this is confirmed by the negligible error bars of *RI*' as seen in other electrolyte combinations (Fig. 5a). To challenge further the capability of TFBG, we performed

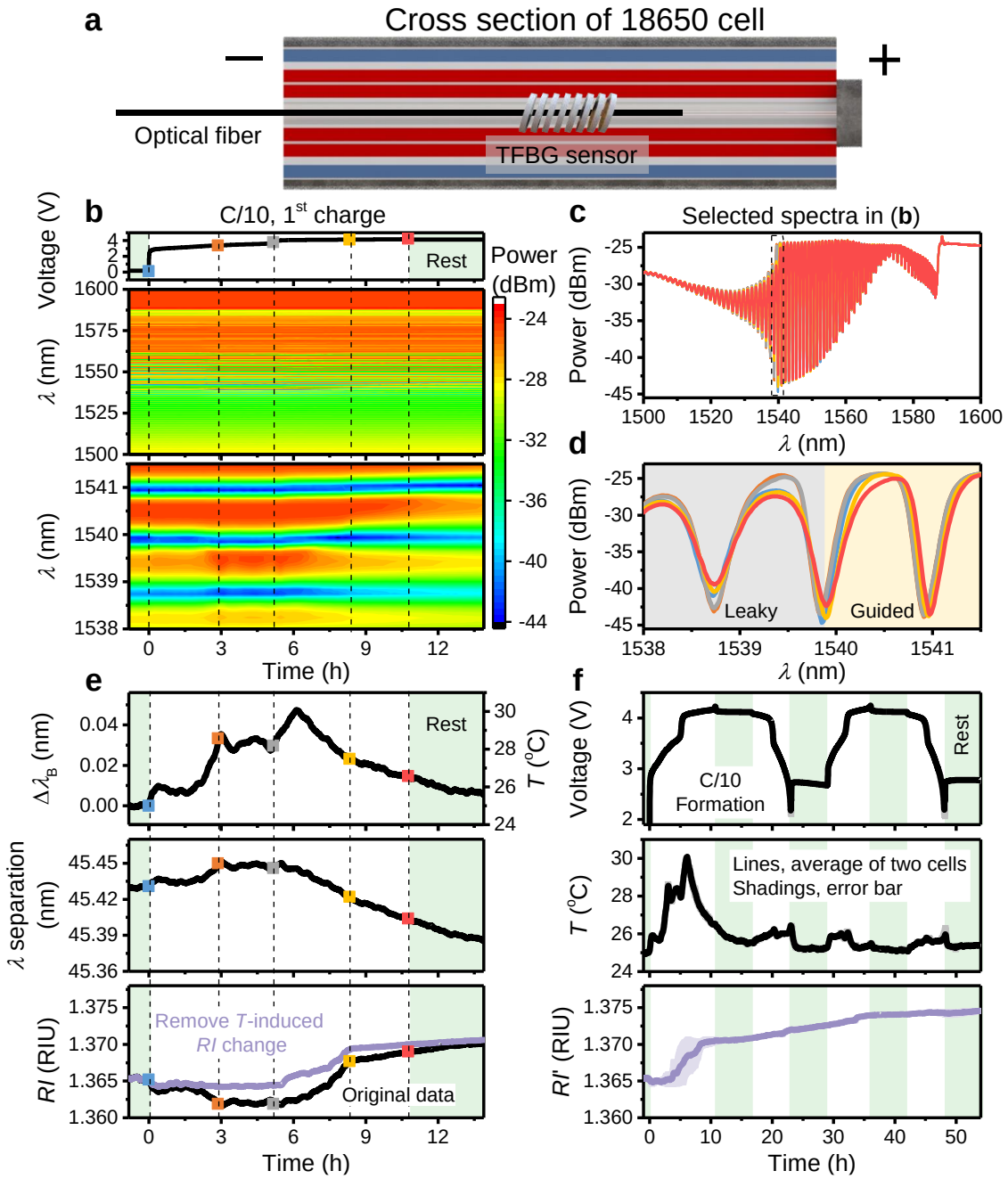

Fig. 3 Decoding *T* and *RI* inside 18650 cells by TFBG. (a) A schematic showing the integration of TFBG into the central void of the jelly roll of an 18650 cell. (b) The temporal voltage (top), full (middle), and enlarged (bottom) TFBG spectrum contours during the first charge of an NVPF/HC 18650 cell containing $NaPF_6$/DMC electrolyte at a current of C/10 to 4.25 V in a 25 °C oven. The green background (top) indicates the rest periods. The scatters and dash lines indicate the positions of selected spectra. (c and d) Full (c) and enlarged (d, dashed rectangle in c) TFBG spectra selected in (b) with the same colors. Similar to Fig. 2a, the grey and yellow backgrounds in (c) indicate the leaky mode and guided cladding mode resonances, respectively. The "ghost" mode in Fig. 2a is invisible here due to the TFBG fabrication. (e) The time-resolved Bragg wavelength shift ($\Delta\lambda_B$, top, left axis), *T* (top, right axis), the wavelength separation between the cladding at ~1,543 nm and Bragg resonances (middle), and *RI* (bottom) of the same cell as (b)'s. In the bottom panel, we subtracted the *T*-induced *RI* change of electrolyte (*RI*', purple line) from the original data (black line). (f) The temporal voltage (top), *T* (middle), and *RI*' (bottom) of two cells with $NaPF_6$/DMC during the first two formation cycles at C/10. The average signals (lines) were calculated together with the error bars (shadings). Two cells do not provide statistically accurate error bars but roughly show the measurements' reproducibility.

galvanostatic intermittent titration technique (GITT) during the formation of cells containing $NaPF_6$/DMC in order to assess the diffusion/reaction kinetics of electrolyte.

Probing degradation and turbidity of electrolyte via TFBG

Fig. 4a shows the temporal voltage profile and the TFBG spectra during the GITT test. Surprisingly, the cell's voltage could not go above 3.25 V (Fig. 4a, top) when resting steps of 4 hours were used, while we can reach 4.25 V in galvanostatic cycling (Fig. 3f, top). Such a difference is the result of copious electrochemically driven decompositions previously reported[8]. This is

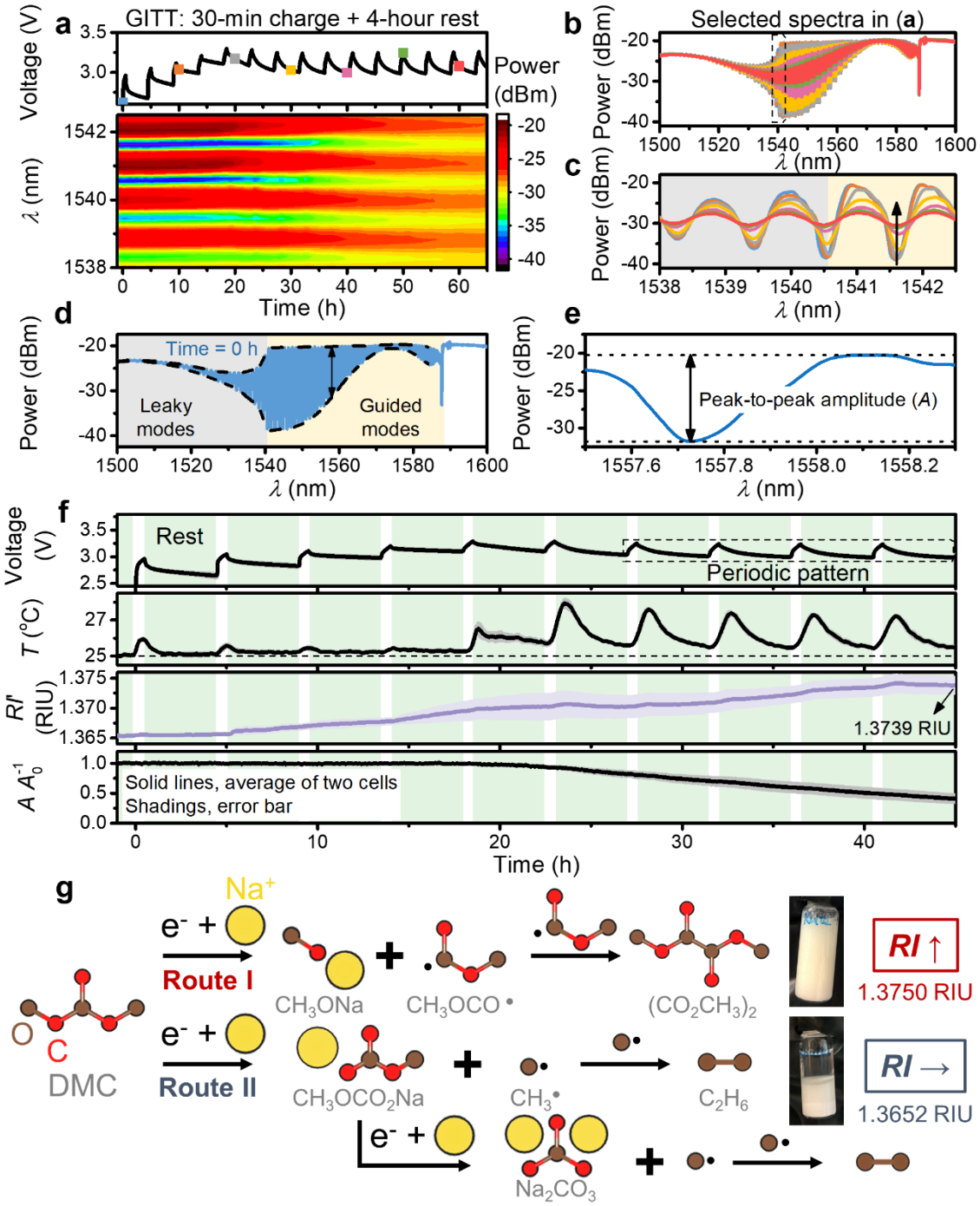

Fig. 4 Sensing electrolyte degradation and turbidity by TFBG. (a) The temporal voltage (top) and enlarged TFBG spectrum contour (bottom) during the GITT (30-min charge followed by 4-hour rest) of an NVPF/HC cell containing $NaPF_6$/DMC electrolyte at a current of C/10 in a 25 °C oven. The voltage rises and decreases during the charge and the rest, respectively. We selected seven points (scatters, top) every 10 hours to show their detailed spectra. (b and c) Full (b) and enlarged (c, dash rectangle in b) spectra of TFBG at the selected points in (a) in the same colors. The arrow in (c) indicates the amplitude suppression of a guided cladding resonance after ~30 hours. (d and e) The definition of peak-to-peak amplitude (*A*) of one guided cladding resonance via the example at 0 hour. Similar to Fig. 2a, the grey and yellow backgrounds represent the leaky mode and guided cladding mode resonances, respectively. The dash lines in (d) are the envelopes of the spectrum, while the arrows indicate *A*. (f) The time-resolved voltage, *T*, *RI'*, and $A\ A_0^{-1}$ of two cells during the GITT test. The green background indicates the rest periods. The average signals (solid lines) were calculated together with the error bars (shadings). The periodic voltage patterns (top) are marked by a dashed rectangle. To examine the exothermic reactions, the dashed line in the *T*'s panel indicates the oven *T* of 25 °C. The "1.3739 RIU" indicates the final *RI* of the test. (g) The proposed reduction pathways of DMC. The "1.3750 RIU" and "1.3652 RIU" corresponds to the refractive indices of artificial "degraded" electrolytes following Route I and Route II, respectively. The "*RI* ↑" and "*RI* →" indicate the *RI* change in comparison to the pristine $NaPF_6$/DMC (~1.3654 RIU).

accompanied by a dramatic change in the TFBG spectrum contours after ~30 hours (Fig. 4a, bottom). Looking into the spectra every 10 hours (Fig. 4b and c), the amplitudes of most of the cladding resonances simultaneously decrease after ~30 hours. This response is different from the gradual *RI* change in liquid solutions (Fig. 2a, 3c, 3d, and S7) but rather similar to the presence of particles on the cladding[30], for example, by taking a TFBG from a sucrose solution to air with some sucrose remains (Fig. S7). Therefore, the dramatic amplitude changes in Fig. 4b and c likely pertain to the excessive depletion of dimethyl carbonate (DMC) and the subsequent precipitation of solid particles such as by-products, which could then enter the evanescent field of TFBG or even be deposited on the cladding. To verify this hypothesis, we utilized the scanning electron microscope (SEM) together with energy-dispersive X-ray spectroscopy (EDX) mapping for the fibers before and after the GITT test. Visibly, some materials, which were rich in Na, P, F, and O, etc., were deposited on the fiber after the test (Fig. S8). This motivates us to find a measurable that reflects the turbidity of electrolytes via the particulates near the TFBG's cladding while being transparent to the change in *RI*. We found that the peak-to-peak amplitude of a guided cladding mode (*A*, Fig. 4d and e) meets this *RI*-immune condition (Fig. S9). Thus, A that solely manifests the photonic energy loss due to the scattering or absorption of particles was taken as the metric reflecting the turbidity of electrolytes. However, for easier comparison, *A* is further normalized to the pristine amplitude (A_0, before electrochemical tests) as $A\ A_0^{-1}$.

Bearing this in mind, we collected the TFBG spectra from two cells and extracted the time-resolved *T*, *RI*', and $A\ A_0^{-1}$ (Fig. 4f). The periodic voltage patterns are spotted at ~3.1 V (dash rectangle), indicating repeated redox processes. Meanwhile, the peaks in temperature suggest intense exothermic chemical reactions as expected when cells are activated. Besides, the $A\ A_0^{-1}$ rapidly approaches zero upon these repeated redox processes, implying the severe saturation of solid particles in the electrolyte. Interestingly, the patterns are absent in the galvanostatic charge in Fig. 3f, implying the critical role of the 4-hour rest with respect to the SEI, in agreement with our previous study reporting soluble SEI in $NaPF_6$/DMC electrolyte[8]. We thus inferred that with the additional 4-hour rest, the severe dissolution of SEI could not prevent the continuous degradation of the electrolyte, hence by the same token, the formation of solid particles was detected by TFBG.

To further understand the decomposition mechanism of DMC, we recalled the proposed reduction pathways of DMC[8] in Fig. 4g and prepared the DMC-based solutions saturated with by-products (sodium methoxide, sodium methyl carbonate, and dimethyl oxalate). We measured their *RI* (Table S1) and found that the additions of saturated sodium methoxide or sodium methyl carbonate slightly decreased the *RI* by $<2\times10^{-4}$ RIU, while it is increased by $\sim1.9\times10^{-2}$ RIU with dimethyl oxalate. These results suggest the possible formation of dimethyl oxalate (and sodium methoxide) through Route I (Fig. 4g) when *RI* increases, for example, after the 2nd-4th titrations between 3.0 and 3.2 V in Fig. 4f. To further explore whether the monitoring of *RI* can help to determine the occurring reaction pathway, we mimicked the two reaction routes in Fig. 4g. Namely, we prepared artificially "degraded" electrolyte solutions by replacing DMC with the required amount of either sodium methoxide + dimethyl oxalate or sodium methyl carbonate + sodium carbonate that are formed in GITT cells after each step assuming that all the passed electrons are used for electrolyte decomposition through Route I and Route II, respectively (Note S1 and Fig. S10). Interestingly, the as-prepared "degraded" electrolytes give *RI*s of ~1.3750 and ~1.3650 RIU at 25 °C, corresponding to Routes I and II (Fig. 4g), respectively, which indicates that among the previously reported electrolyte decomposition pathways, Route I is most likely because we measured an *RI* of 1.3739 RIU for our electrochemical cells. The Route I is further confirmed by the *ex situ* FT-IR spectra showing the formation of sodium methoxide and dimethyl oxalate (Fig. S11). Besides, it is worth mentioning that the visualized turbidity of the "degraded" electrolytes (Fig. 4g and S10) is consistent with the suppressed resonance amplitudes in Fig. 4b and the vastly reduced $A\ A_0^{-1}$ after the test in Fig. 4f.

Generalization to other electrolytes and implication for capacity loss

TFBG's sensors were next injected in various 18650 Na-ion cells filled with other electrolyte formulae, including 1 M $NaPF_6$ in ethylene carbonate (EC) and DMC (v.:v. = 1:1) with 3 wt.% vinylene carbonate (VC) (denoted as "NP30+VC") and 1 M $NaPF_6$ in EC:DMC:propylene carbonate (PC) (1:1:1 in volume) with 3 wt.% VC, 3 wt.% succinonitrile (SN), 0.5 wt.% sodium (oxalate) difluoro borate (NaODFB), and 0.2 wt.% tris(trimethylsilyl) phosphite (TMSPi) (denoted as "Magic C"). Fig. 5a shows the time-resolved voltage, *T*, and Δ*RI*' (relative to the pristine *RI* of the electrolytes, rather than *RI*' for easier comparison) of two 18650 NVPF/HC cells for each electrolyte during the 1st cycle at C/10. The slight voltage shifts in the time scale between different electrolytes (Fig. 5a, top, arrow) manifest the presence of copious side reactions[8]. This is accompanied by the decrease in temperature signals from $NaPF_6$/DMC to NP30+VC and Magic C (Fig. 5a, middle), implying the suppression of parasitic reactions with proper co-solvent and additives as confirmed by exploiting the d*V*/d*Q* plot in Fig. S12. Interestingly, NP30+VC and Magic C also give less Δ*RI*' change than $NaPF_6$/DMC (Fig. 5a, bottom), confirming the positive attributes of additives against electrolyte degradation. At this stage, the *RI*' information may be further combined with the optical calorimetry[4] and the theoretical calculations of dielectric constant[31] (square of *RI*) to investigate the chemistries of SEI formation, but it is beyond the scope of this paper.

To further access the benefit of TFBG for cell monitoring, we plotted the charge capacity (or capacity retention), Δ*RI*', and $A\ A_0^{-1}$ against the cycle number in Fig. 5b and c. During the formation cycles (Fig. 5b), as expected, $NaPF_6$/DMC delivers the highest 1st charge capacity and the fastest decay due to the worst SEI formation[8]. Meanwhile, from TFBG data we can deduce a dramatic increase in Δ*RI*' and a decrease in $A\ A_0^{-1}$, pertaining to the severe degradation and particle saturation in the electrolyte, respectively. Such changes in Δ*RI*' and $A\ A_0^{-1}$ are reduced in NP30+VC and Magic C, which show nearly the same

capacities. Turning to capacity retention (Fig. 5c), $NaPF_6$/DMC immediately loses ~15% capacity after 10 cycles, and this is accompanied by a considerable increase in $\Delta RI'$ and a decrease in $A\ A_0^{-1}$. The capacity retentions are similar among the other two electrolytes; however, the information from TFBG is quite different. The $\Delta RI'$ and $A\ A_0^{-1}$ remain nearly unchanged in Magic C, while the $\Delta RI'$ of NP30+VC increases concomitantly with a gradual decrease of $A\ A_0^{-1}$ to ~0.8, meaning the deterioration of electrolytes involving particle nucleation (*i.e.*, the increased turbidity).

Furthermore, to know whether TFBG's observables enable to track capacity retention, we plotted independently the

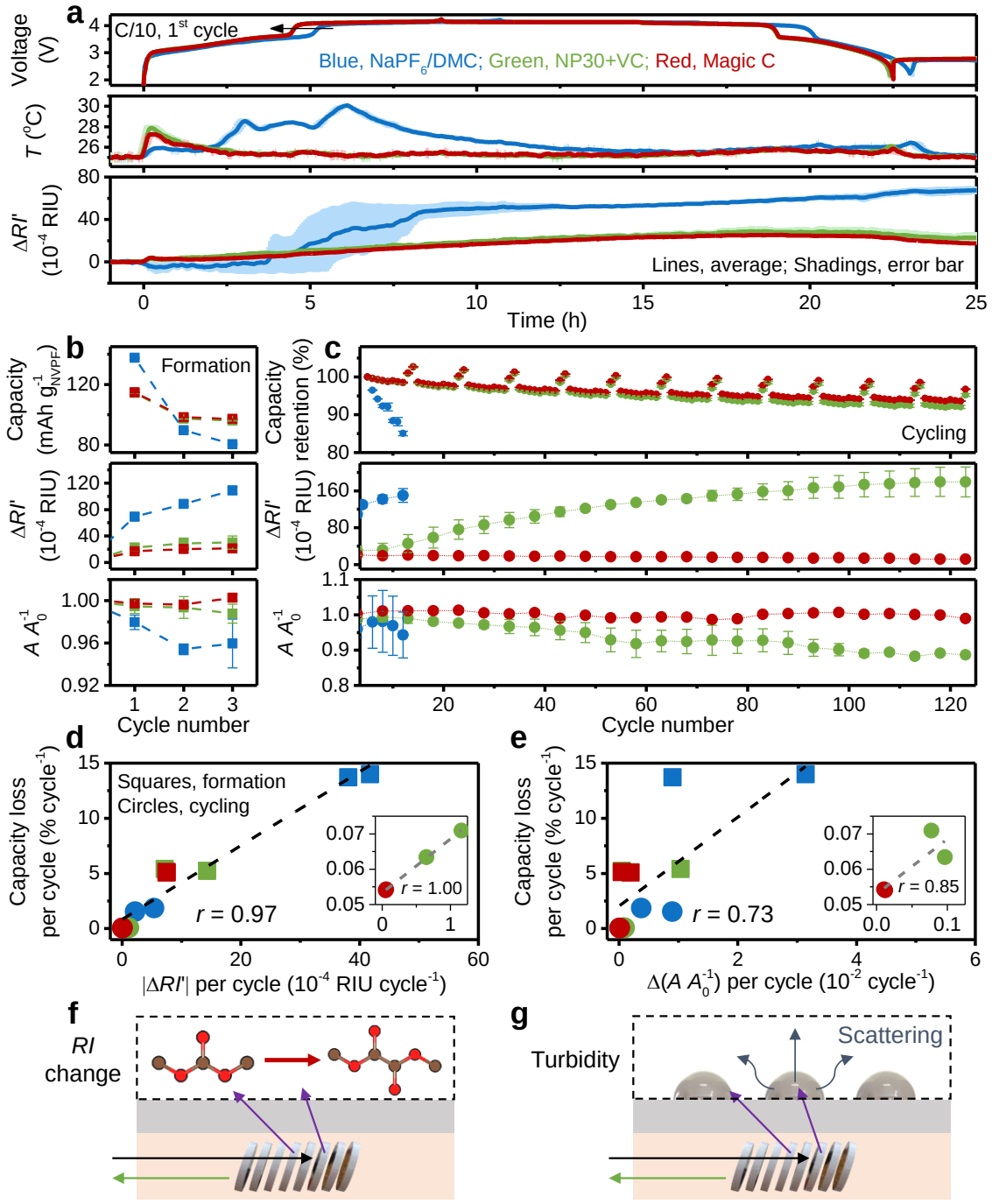

Fig. 5 Methodology generalization and the implication for capacity loss. (a) The temporal voltage (top), *T* (middle), and $\Delta RI'$ (bottom) of two cells for each electrolyte, including $NaPF_6$/DMC (blue), NP30+VC (green), and Magic C (red), during the first formation cycle at C/10 with 6-hour rest between charge and discharge in a 25 °C oven. The average signals (lines) were calculated together with the error bars (shadings). The arrow (top) indicates the shift of voltage profiles with electrolyte additives. (b and c) The charge capacity (b, top), charge capacity retention (c, top, relative to the 5th cycle), $\Delta RI'$ (middle), and $A\ A_0^{-1}$ (bottom) as a function of cycle number during the formation at C/10 (b) and the cycling test at 1C (c). The charge capacities were selected to reflect the irreversibility during the first cycle. Except for $NaPF_6$/DMC, C/10 was applied every ten cycles to access the full remaining capacity. To avoid complicating the figures with all the data, error bars are given based on the two cells' results. Dashed lines are provided as a guide to the eyes. The corresponding TFBG spectra are shown in Fig. S13. (d and e) The correlation between the capacity loss per cycle and the absolute $\Delta RI'$ ($|\Delta RI'|$) per cycle (d) or the $A\ A_0^{-1}$ change ($\Delta(A\ A_0^{-1})$) per cycle (e). Squares and circles represent the formation and cycling results, respectively. Note that the colors for different electrolytes are identical to (a)'s. The insets are the cycling results of NP30+VC and Magic C. The black and grey dash lines represent the linear regressions of the total and inset data, respectively. (f and g) The schematics showing the phenomena of *RI* change arising from the (electro-)chemical reactions (f) and the turbidity (g), corresponding to RI' and $A\ A_0^{-1}$, respectively.

capacity loss per cycle against the changes in $\Delta RI'$ and $A\ A_0^{-1}$ during both formation (squares) and cycling (circles) tests (Fig. 5d and e). We further exploited the data by calculating the Pearson correlation coefficient (r), see the equation in the reference[32]. Remarkably, we found r of 0.97 for the $\Delta RI'$, indicating a strong correlation between the capacity loss and $\Delta RI'$. This contrasts with the moderate relationship (r = 0.73) between the capacity loss and $A\ A_0^{-1}$, most likely due to the turbidity inhomogeneity. Additionally, we computed the r of cycling data from 5th to 123rd cycles of NP30+VC and Magic C (Fig. 5d and e, insets). We found r of 1.00 and 0.85 for $\Delta RI'$ and $A\ A_0^{-1}$, respectively, which according to statistical criteria[33] indicate that these metrics are strongly correlated to the capacity loss. Altogether, these two TFBG metrics spot different aspects, namely, electrolyte deterioration via changes in RI (Fig. 5f) and turbidity (Fig. 5g), hence providing valuable inputs for the data-driven battery management system.

Discussions and conclusions

We have demonstrated that TFBG sensors can be used for simultaneous operando deciphering of temperature and electrolyte refractive index in practical 18650 Na-ion batteries under real working conditions. These sensors, that couple the core and cladding modes via a controlled tilt of the grating planes, provide a more simplified, explicit, and reproducible method to measure refractive index than the previous optical sensors relying on the inscribing of grating on cladding-etched fibers[26]. Moreover, we provide evidence that TFBG's can assess the turbidity of electrolytes while also enabling to identify the (electro-)chemical reaction pathways during the SEI formation, both of which were unattained previously. Lastly, by generalizing the methodology to a few electrolyte formulae, we unravel the strong correlations between the capacity loss and the two electrolyte observables derived from TFBG signals, providing new inputs for artificial intelligence[34] to better understand and predict cell ageing.

Despite these encouraging results, we identify some weaknesses of the current TFBG methodology together with possible curing solutions, that enlists an optimization of the inscription system to minimize the response variance between sensors. This can be done at the engineering level or indirectly by machine learning algorithms on the full spectrum as presently being explored in our group. Equally, to simplify the refractive index analysis and address rapidly the possible wavelength drift, a possible approach could consist in taking a Fast Fourier Transform of the TFBG spectra[35] with a Hanning window as shown in Fig. S14. Besides, to achieve a better reliability of the data (Fig. 5e), we need to carefully control the polarization states of light by polarizer and polarization controller. Also, to tackle the concerns arising from the gold reflector, we are simultaneously optimizing the coating technique and exploring the transmission method. Finally, we have ensured the inertness of the TFBG's sensors to the targeted battery environment in terms of chemical reactivity with the presently used electrolytes by conducting SEM on the fibers (Fig. S8g,h) and examining their spectra (Fig. S15) after the tests. Nevertheless, more comprehensive studies under harsh conditions are still in need.

Overall, we present the feasibility and diversity of TFBGs to monitor the state of electrolytes in an operando way. Since each resonance responds differently to RI, T, and ε (Fig. 2c, 2d, and S3), the multiple modes of TFBG offer a viable platform to acquire at the same time multiple observables that can be decoupled. Along that line and in light of our previous work[4], we are presently exploring to write TFBG in MOF to monitor internal pressure as a n^{th} observable. New opportunities that combine inputs of surface plasmon resonance-based TFBG sensors with simulations and quantum calculations can also be envisioned as well for decoding delicate chemical information at the molecular scale inside the battery. The further combination with new processing innovations for simplifying the inscribing of such sensors on the fiber as well as major advance in data collection and treatment algorithms should help in realizing a "lab-on-fiber" analytical platform for field battery monitoring.

Methods

Fabrication of TFBG

Gratings were inscribed in hydrogen-loaded fiber (SMF-28, Corning) using 193 nm excimer laser (COMPexPro110), and a phase mask with pitch of 1098.19 nm. The applied energy of the excimer laser was 115 mJ with a repetition rate of 30 Hz and a scan velocity of 20 µm s^{-1}. During grating fabrication, we kept the phase mask and the fiber in parallel and rotated them at an angle of 16° around the axis of the laser beam. Note that the tilted angel of 16° were determined by our simulation package to cover the working range of electrolytes. The lengths of the grating region were ~15 mm in length, with the Bragg resonance at 1,589 nm. Finally, the sensor is specially designed with a gold mirror with a thickness of ~100 nm on the flattened fiber end by using the sputtering technique (TRI-S500, Polaron Instruments). Comparing to other metal reflectors such as silver, copper, Au layer is more stable (*e.g.,* against oxidation) and has a high reflection coefficient near 1550 nm wavelength. Note that we carefully protected the grating region from the gold coating to elude the surface plasmon resonance[25].

TFBG sensors in response to *RI, T, ε, and P*

The RI measurements of TFBGs were benchmarked by a series of sucrose (Sigma-Aldrich, BioXtra, ⩾99.5%) solutions from 10 to 50 wt.%. in 2 wt.% increments in distilled water. TFBGs were immersed in the solutions without bending or strain, and the response spectra were recorded by the optical interrogator. The RIs of the sucrose solutions were measured by the commercial refractometer (AR200, Reichert Technologies; resolution: ±0.0001 RIU). To test the accuracy of TFBG together with the correction method of wavelength separation, another group of sucrose solutions (from 5 to 45 wt.% in 10 wt.% increments) was prepared, and their RIs were successively measured by the TFBGs and AR200 for comparison (Fig. S5c). Note that a reference point of the distilled water was taken prior to each measurement. While the reference correction was

automatically done in AR200, the calibration curves of TFBG were corrected relative to the reference point in order to remove the possible drifts arising from the environment or TFBG itself (Fig. S5). Note that we calibrated each TFBG individually.

The thermal calibrations of TFBGs were done in the oven (IPP110, Mermmet) from 10 to 60 °C with a step of 10 °C and a rest time of 4 hours in each step. The temporal spectra were recorded to investigate the thermal response of each resonance.

The ε calibration was conducted on two translation stages (XW-13-0.25, Lianyi) by fixing two ends of 10-cm fiber containing the 15-mm tilted grating region. While keeping one stage fixed, we moved the other stage by a step of 10 μm (*i.e.*, 100 με) until 50 μm (*i.e.,* 500 με), and the spectra were recorded by an interrogator (FS22SI, HBM) at each step after the strain was kept for 30 s.

The *P* calibration was done using a pressure chamber (length: 300 mm; inner diameter: 50 mm) filled with water. We increased the pressure from 0 to 20 bar in 2 bar increments, and we recorded the spectra by the optical spectrum analyser (AQ6370, YOKOGAWA) at each step after 30-s stabilization. A maximal pressure 20 bar was selected here, considering the pressure limit of safety device for 18650 cells.

Electrolyte preparation

$NaPF_6$, DMC, EC, PC, VC, SN, and TMSPi were purchased from Stella, E-Lyte, Duoduo Chem, Solvionic, TCI Chemicals, Acros Organics, and TCI Chemicals, respectively. NaODFB was synthesized in our group[36]. The solvents of DMC, EC, and PC were dried in activated molecular sieves. Sodium methoxide and dimethyl oxalate were obtained from Alfa Aesar. We synthesized sodium methyl carbonate as previously reported[8], see the Fourier-transform infrared spectroscopy (FT-IR, by Nicolet™ iS5, Thermo Scientific) and liquid-state nuclear magnetic resonance (NMR, by 7.046 T Avance III HD with a 5 mm HX(F) probe head, Bruker) results in Fig. S16.

Integration of TFBG into the 18650 cells

The NVPF/HC 18650 cells were provided by TIAMAT company, which were hermetically sealed in the dry room without electrolyte filling. An 0.8-mm hole was drilled on the center of the negative pole. The electrical resistance was checked before and after drilling to make sure that there was no short circuit. The drilled cells were subsequently dried in the glass oven (B-585, BÜCHI) under vacuum at 80 °C overnight. These cells were then transferred into the Ar-filled glove box and filled with ~5.3-mL electrolyte through the 0.8-mm hole. The TFBG was pre-bonded with a needle by epoxy for future reuse. The TFBG was inserted into the central void of jelly roll via the 0.8-mm hole with the grating region close to the negative pole (Fig. S17). They were then sealed by epoxy, which took 24 hours for curing. The cells with TFBGs were taken out of the glove box, installed into the homemade cabinets[4] in a temperature-controlled oven, and connected to the potentiostat and optical interrogator. The cells were kept in the open circuit for ~12 hours to reach the equilibrium state. Each batch of experiments contained two cells for reproducibility examination.

Electrochemical and optical measurements

We used the potentiostat (BCS-815, BioLogic) for the electrochemical signals. The 1C of NVPF/HC is 128 mAh g^{-1} based on the mass of NVPF. The voltage window was 2.00 to 4.25 V. During the 1C cycling, a constant voltage at 4.25 V was applied until the current reached C/5. We utilized the 8-channel interrogator (si255, LUNA) to record the time-resolved TFBG spectra between 1500 and 1600 nm at a rate of 30 or 60 s rather than 1 s to reduce the data amount. Note that the maximal rate of full spectrum measurement of the interrogator is 10 Hz.

Temperature coefficient of *RI*

The TFBG was inserted into a glass bottom containing 4-mL solutions (solvents or electrolytes) in an Ar-filled glove box. We avoided bending or strain on TFBGs to guarantee similar conditions to the calibrations. The interfaces were sealed by either rubber or epoxy for airtightness. The glass bottom with a TFBG was then taken out of the glove box and placed into a temperature control oven. We waited four hours for the system to reach thermal equilibrium and rose the temperature to 40 °C; meanwhile, the temporal TFBG's spectra were collected, which provided the real-time *T* and *RI* of the solutions.

SEM

For Fig. S8, the fiber after GITT was taken out from the cells by polishing the epoxy. Because the target was to examine whether there were some particulate depositions, we conducted the recovery in the air rather than a protective atmosphere. For the cleaned sample, we applied ethanol with wipes (Kimtech). Prior to being pasted on the carbon tape for SEM, those samples were coated with gold by the plasma sputtering coater (GSL-1100X-SPC-12, MTI). We used a SEM (FEI Magellan) equipped with an energy-dispersive X-ray spectroscopy (EDX) detector (Oxford Instruments).

Author Contributions

J.H., T. G., and J.-M. T. conceived the idea and designed the experiments. X. H. and T. G. fabricated the TFBGs and conducted the strain and pressure calibrations. J. H. performed the experiments and the data analysis. F. L., T.G., and X. H. helped to interpret the optical data. J.H. and J.-M. T. wrote the paper with the inputs from all authors. C.G. and L.A.B helped to reviewed and edited the paper.

Conflicts of interest

The authors declare no competing financial interests.

Acknowledgements

J.-M.T., J.H., and L.A.B. acknowledge funding from the European Research Council (ERC) (FP/2014)/ERC Grant-Project 670116-ARPEMA, DIM RESPORE, and the International Balzan Prize Foundation. T. G. acknowledge funding from the Key Program of National Natural Science Foundation of China (No. 62035006) and the Guangdong Outstanding Scientific Innovation

Foundation (No. 2019TX05X383). We thank Tuncay KOÇ, Nicolas DUBOUIS, and Parth DESAI for their help in SEM, NMR, and d*V*/d*Q* analysis, respectively. We also gratefully thank Kaiwei LI for the valuable discussion, Zhengyong LIU and Hwa-Yaw TAM for their assistance in the pressure calibration. We appreciate the inspiring discussion on data science with Stephane MALLAT and Loic VALLANCE. We are indebted to TIAMAT for providing the NVPF/HC 18650 cells as well as Faurecia for supporting part of this work.

References

1. M. Armand and J.-M. Tarascon, *Nature*, 2008, **451**, 652-657.
2. D. Larcher and J. M. Tarascon, *Nat. Chem.*, 2015, **7**, 19-29.
3. C. Grey and J.-M. Tarascon, *Nat. Mater.*, 2017, **16**, 45-56.
4. J. Huang, L. A. Blanquer, J. Bonefacino, E. R. Logan, D. A. Dalla Corte, C. Delacourt, B. M. Gallant, S. T. Boles, J. Dahn, H.-Y. Tam and J. M. Tarascon, *Nat. Energy*, 2020, **5**, 674-683.
5. L. Downie, S. Hyatt and J. Dahn, *J. Electrochem. Soc.*, 2016, **163**, A35-A42.
6. T. Ohzuku, H. Tomura and K. Sawai, *J. Electrochem. Soc.*, 1997, **144**, 3496.
7. C. J. Bae, A. Manandhar, P. Kiesel and A. Raghavan, *Energy Technology*, 2016, **4**, 851-855.
8. G. Yan, D. Alves-Dalla-Corte, W. Yin, N. Madern, G. Gachot and J.-M. Tarascon, *J. Electrochem. Soc.*, 2018, **165**, A1222-A1230.
9. C. Cometto, G. Yan, S. Mariyappan and J.-M. Tarascon, *J. Electrochem. Soc.*, 2019, **166**, A3723-A3730.
10. J. Huang, X. Guo, X. Du, X. Lin, J.-Q. Huang, H. Tan, Y. Zhu and B. Zhang, *Energy Environ. Sci.*, 2019, **12**, 1550-1557.
11. S. Laruelle, S. Pilard, P. Guenot, S. Grugeon and J.-M. Tarascon, *J. Electrochem. Soc.*, 2004, **151**, A1202.
12. Y. Jin, N.-J. H. Kneusels, P. C. Magusin, G. Kim, E. Castillo-Martínez, L. E. Marbella, R. N. Kerber, D. J. Howe, S. Paul and T. Liu, *J. Am. Chem. Soc.*, 2017, **139**, 14992-15004.
13. R. Day, J. Xia, R. Petibon, J. Rucska, H. Wang, A. Wright and J. Dahn, *J. Electrochem. Soc.*, 2015, **162**, A2577.
14. A. Louli, A. Eldesoky, R. Weber, M. Genovese, M. Coon, J. deGooyer, Z. Deng, R. White, J. Lee and T. Rodgers, *Nat. Energy*, 2020, **5**, 693-702.
15. Z. Deng, Z. Huang, Y. Shen, Y. Huang, H. Ding, A. Luscombe, M. Johnson, J. E. Harlow, R. Gauthier and J. R. Dahn, *Joule*, 2020, **4**, 2017-2029.
16. P. Desai, J. Huang, H. Hijazi, L. Zhang, S. Mariyappan and J. M. Tarascon, *Adv. Energy Mater.*, 2021, 2101490.
17. J. Huang, L. ALBERO Blanquer, C. Gervillie and J.-M. Tarascon, *J. Electrochem. Soc.*, 2021, **168**, 060520.
18. A. Ghannoum, R. C. Norris, K. Iyer, L. Zdravkova, A. Yu and P. Nieva, *ACS Appl. Mater. Interfaces*, 2016, **8**, 18763-18769.
19. E. Miele, W. Dose, I. Manyakin, M. Frosz, C. Grey, J. Baumberg and T. Euser, 2020.
20. S. W. James and R. P. Tatam, *Meas. Sci. Technol.*, 2003, **14**, R49.
21. J. Albert, L. Y. Shao and C. Caucheteur, *Laser & Photonics Reviews*, 2013, **7**, 83-108.
22. L. Marrec, T. Bourgerette, E. Datin, N. Ferchaud, B. Pucel, L. Quetel, C. Renault and D. Tregoat, 2005.
23. T. Guo, F. Liu, B.-O. Guan and J. Albert, *Optics & Laser Technology*, 2016, **78**, 19-33.
24. Y. Yuan, T. Guo, X. Qiu, J. Tang, Y. Huang, L. Zhuang, S. Zhou, Z. Li, B.-O. Guan and X. Zhang, *Anal. Chem.*, 2016, **88**, 7609-7616.
25. J. Lao, P. Sun, F. Liu, X. Zhang, C. Zhao, W. Mai, T. Guo, G. Xiao and J. Albert, *Light: Science & Applications*, 2018, **7**, 1-11.
26. A. Nedjalkov, J. Meyer, A. Gräfenstein, B. Schramm, M. Angelmahr, J. Schwenzel and W. Schade, *Batteries*, 2019, **5**, 30.
27. C.-F. Chan, C. Chen, A. Jafari, A. Laronche, D. J. Thomson and J. Albert, *Appl. Opt.*, 2007, **46**, 1142-1149.
28. R. Waxler and C. Weir, *Journal of research of the National Bureau of Standards. Section A, Physics and chemistry*, 1963, **67**, 163.
29. C. F. Snyder and A. T. Hattenburg, *Refractive indices and densities of aqueous solutions of invert sugar*, National Bureau of Standards, 1963.
30. F. Liu, X. Zhang, T. Guo and J. Albert, *APL Photonics*, 2020, **5**, 076101.
31. J. Self, B. M. Wood, N. N. Rajput and K. A. Persson, *J. Phys. Chem. C*, 2018, **122**, 1990-1994.
32. R. P. David Freedman, Roger Purves, *Statistics*, W. W. Norton & Company, London, 2007.
33. R. Taylor, *Journal of diagnostic medical sonography*, 1990, **6**, 35-39.
34. T. Vegge, J. M. Tarascon and K. Edström, *Adv. Energy Mater.*, 2021, 2100362.
35. S. Maguis, G. Laffont, P. Ferdinand, B. Carbonnier, K. Kham, T. Mekhalif and M.-C. Millot, *Optics Express*, 2008, **16**, 19049-19062.
36. G. Yan, K. Reeves, D. Foix, Z. Li, C. Cometto, S. Mariyappan, M. Salanne and J. M. Tarascon, *Adv. Energy Mater.*, 2019, **9**, 1901431.